Gravitational Bar and Spiral Arm Torques from K_s-band Observations and Implications for the Pattern Speeds

D. L. Block[1], R. Buta[2], J. H. Knapen[3], D. M. Elmegreen[4], B. G. Elmegreen[5], & I. Puerari[6]

ABSTRACT

We have obtained deep near-infrared K_s-band William Herschel Telescope observations of a sample of 15 nearby spiral galaxies having a range of Hubble types and apparent bar strengths. The near-infrared light distributions are converted into gravitational potentials, and the maximum relative gravitational torques due to the bars and the spirals are estimated. We find that spiral strength, Q_s, and bar strength, Q_b, correlate well with other measures of spiral arm and bar amplitudes, and that spiral and bar strengths also correlate well with each other. We also find a correlation between the position angle of the end of the bar and the position angle of the inner spiral. These correlations suggest that the bars and spirals grow together with the same rates and pattern speeds. We also show that the strongest bars tend to have the most open spiral patterns. Because open spirals imply high disk-to-halo mass ratios, bars and spirals most likely grow together as a combined disk instability. They stop growing for different reasons, however, giving the observed variation in bar-spiral morphologies. Bar growth stops because of saturation when most of the inner disk is in the bar, and spiral growth stops because of increased stability as the gas leaves and the outer disk heats up.

Subject headings: galaxies: spiral; galaxies: photometry; galaxies: kinematics and dynamics; galaxies: structure

1. Introduction

The evolution of disk galaxies is significantly influenced by the main features within their disks, notably spirals and bars. In turn, galactic evolution also significantly influences the evolution, morphology, and dynamics of these features. Bars at the present epoch can be found in about 70%

of massive disk galaxies using near-infrared images (Sellwood & Wilkinson 1993; Knapen et al. 1999; Eskridge et al. 2000). The fraction is somewhat lower on optical images.

The gravitational torque method (GTM, Buta & Block 2001) was developed to quantify bar strength. The idea is to transform a deprojected near-infrared image of a spiral galaxy into a gravitational potential, and then compute the ratio of the tangential force to the mean radial force as a function of position in the plane of the galaxy. The potential is derived from Poisson's law after assuming an exponential vertical density law and a constant mass-to-light ratio (Quillen, Frogel, and González 1994). The mean radial force represents the axisymmetric background due to the bulge, disk, and bar. A fully quantitative measure of bar strength can be defined from the maximum of the tangential-to-radial force ratio, as long ago suggested by Sanders & Tubbs (1980) and

[1]School of Computational and Applied Mathematics, University of the Witwatersrand, P.O. Box 60, Wits, Gauteng 2050, South Africa

[2]Department of Physics & Astronomy, University of Alabama, Box 870324, Tuscaloosa, AL 35487

[3]Centre for Astrophysics Research, Science & Technology Research School, University of Hertfordshire, Hatfield, Herts AL10 9AB, U.K.

[4]Department of Physics & Astronomy, Vassar College, Box 745, Poughkeepsie, NY 12604

[5]IBM Research Division, T. J. Watson Research Center, P. O. Box 218, Yorktown Heights, NY 10598

[6]Instituto Nacional de Astrofísica, Optica y Electrónica, Apdo, Postal 51 y 216, 72000, Puebla, Pue., México

Combes & Sanders (1981). The maximum force ratio is equivalent to the maximum gravitational torque per unit mass per unit square of the circular speed. The GTM has been applied to large samples of galaxies in several recent studies (Block et al. 2001, 2002; Laurikainen, Salo, & Rautiainen 2002; Laurikainen & Salo 2002; Buta, Laurikainen, & Salo 2004, hereafter BLS; Laurikianen, Salo, & Buta 2004a; Laurikainen et al. 2004b). In general, the GTM has an advantage over other methods previously used to define bar strength because it is based on the forcing due to the bar itself and not just on the bar's apparent shape. The relative bar torque is a good measure of the importance of non-axisymmetric forces, which play a role in gas accretion, spiral arm generation, and overall disk evolution.

Studies at optical wavelengths suggested that early-type barred galaxies are associated with grand design spiral structure because the bars end near their own corotation resonances, and at this point they have enough torque to drive corotating spiral waves outward into the disk (e.g., Elmegreen & Elmegreen 1985, 1989). Late-type bars could have different bar and spiral pattern speeds, as observed for NGC 925 (Elmegreen, Wilcots & Pisano 1998).

The interaction between bars and spirals is not well understood observationally because most studies have been based on optical images, which are confused by dust and star formation. We have shown, for example, that K-band spirals often look different from optical spirals with regard to pitch angle, continuity, and symmetry (Block & Wainscoat 1991; Block et al. 1999). Because the light distribution at 2.2μm emphasizes the mass distribution in the old disk, the near-infrared spirals are more important for bar driving than the optical spirals.

Buta, Block, & Knapen (2003, hereafter BBK) have shown that it is possible to use straightforward Fourier techniques to separate the luminosity distributions of bars and spirals (see also Lindblad, Lindblad, & Athanassoula 1996). The GTM is then used to derive maximum relative torques for each nonaxisymmetric feature alone, thereby allowing us to examine in a quantitative manner the possible correlation between bar and spiral strengths. In this paper, we apply the BBK method to 17 representative disk galaxies covering a range of early to intermediate Hubble types and de Vaucouleurs family classifications. Our goal is to investigate the relation between bar torque and spiral arm amplitude.

2. Observations and Sample

Our sample consists of the 17 galaxies listed in Table 1. These were selected on the basis of Hubble type (range Sab-Scd) and inclination (less than 70°). The absolute blue magnitudes of the galaxies range from -18.3 to -21.4, with an average of -20.5 ± 0.9. Thus, these are massive, high luminosity systems, typical of the bright galaxy population. A range of apparent bar strengths covering the de Vaucouleurs families SA, SAB, and SB was also selected.

Fifteen of our sample galaxies were observed during a total of five nights (2001 September 5, and 2001 October 5–8) with the INGRID camera (Packham et al. 2003) attached to the 4.2-m William Herschel Telescope (WHT). The images were taken in the K-short (2.2μm, or K_s) band, and have a scale of 0.241 arcsec/pix and a field of view approximately 4 arcminutes square. Total on-source exposure times average about 59 min, but ranged from 16 to 100 min (see Table 1). The observing techniques are the same as those described in Knapen et al. (2003). Particularly important is the background subtraction, which was performed by interspersing between small blocks of galaxy observations several exposures of the same length on a blank background field. We estimate the typical sky subtraction error to be on the order of 0.1%-0.2% of the total background. To eliminate bad pixels, columns, and (in the case of the background frames) foreground stars, dithering was used for both the galaxy and background frames. We required deeper than usual exposures at 2μm in order to effectively measure spiral arm torques. The limiting surface brightness and typical signal-to-noise ratio were estimated from our K_s image of NGC 1530 using an independently measured K_s flux listed in the NED. In this image, a 48 min exposure, the signal-to-noise ratio is 2.6 at a surface brightness level $\mu_{K_s} = 20.0$ mag arcsec^{-2}. Typical 1σ background noise is 21.0 mag arcsec^{-2}, down to around 21.3 mag arcsec^{-2} for our longest exposures.

In addition to the 15 WHT objects, our anal-

ysis includes two southern strongly-barred galaxies, NGC 1365 and NGC 1433, which were part of previously published studies. These were observed with the CTIO Infrared Imager (CIRIM) attached to the 1.5-m telescope of Cerro Tololo Inter-American Observatory (CTIO) and have a scale of $1''14$ pix^{-1}. Details of the observations of NGC 1365, observed at K, are provided by Regan & Elmegreen (1997), while those for NGC 1433, observed at H, are provided by Buta et al. (2001).

3. Bar/Spiral Separation

The GTM as used in previous studies involves the derivation of the maximum tangential-to-radial force ratio, a single number that characterizes the strength of nonaxisymmetric perturbations in a galaxy. BB01 inspected the two-dimensional ratio ("butterfly") maps of tangential force F_T to mean radial force F_{0R} to insure that this maximum was mostly measuring a bar for their 36 galaxies. Hence, they called the force ratio maximum Q_b. A more automated approach was used by Laurikainen, Salo, & Rautiainen (2002) and Block et al. (2002) whereby the maximum force ratio is derived from the radial variation of the maximum ratio $Q_T = |F_T/F_{0R}|_{\max}$. Depending on the relative importance of the bar and the spiral, the maximum Q_T could be in the bar or the spiral region. For this reason, BBK proposed calling the maximum force ratio Q_g to remove any ambiguity about what it represents. Since Q_g in a barred galaxy could be affected by spiral arm torques, we cannot use Q_g alone to assess whether stronger bars correlate with stronger spirals. Instead, we need to use the special technique outlined by BBK, a Fourier-based method that separates the torques due to a bar from those due to a spiral. However, unlike estimates of Q_g, bar/spiral separation is not automated but depends on an iterative procedure.

In this section, we carry out the BBK separation procedure on each sample galaxy, and then compare the results with estimates based on arm-interarm and bar-interbar contrasts. The galaxy images are deprojected using mainly RC3 (de Vaucouleurs et al. 1991) orientation parameters, with revisions for three galaxies based on isophotal ellipse fits (NGC 6951, 7723) or kinematic parameters (NGC 1530, Regan et al. 1996). Gravita-

tional potentials are evaluated using the method of Quillen, Frogel, & González (1994), under the assumptions of a constant near-IR mass-to-light ratio and an exponential vertical scaleheight h_z estimated from the radial scalelength h_R and the type-dependent ratio h_R/h_z from de Grijs (1998). A revised lookup table for the vertical dimension (see BBK) was used that did not involve any gravity softening.

3.1. Application of the BBK Technique

In the BBK approach, relative Fourier intensity amplitudes are derived from the deprojected near-infrared images. In the inner parts of the galaxy, we assume that the nonaxisymmetric amplitudes are due entirely to the bar, while past a radius r_m (where m is the Fourier azimuthal index) the observed amplitudes are due to a combination of the bar and the spiral. We assume that the even relative Fourier amplitudes due to the bar decline past the maximum at r_m in the same manner as they rose to that maximum. A Fourier image of the bar is constructed and removed from the original image, to give a spiral plus disk image. Then the $m=0$ Fourier image is added back to the bar image to give the bar plus disk image. We convert each of these images into gravitational potentials, and derive maps of the ratio of the tangential force to the mean background radial force, the latter being defined by the $m=0$ Fourier image. From these ratio maps, we derive the maximum force ratios Q_b due to the bar and Q_s due to the spiral arms. In practice, we base our analysis entirely on Fourier-smoothed images using terms up to $m=20$. BBK fully discuss the pitfalls and uncertainties in this method of separation, but it is probably the most straightforward approach one can use for this purpose.

Although BBK illustrated the technique using a fairly symmetric barred spiral (NGC 6951), our present sample includes one asymmetric barred spiral, NGC 7741, that necessitated special attention to odd Fourier amplitudes in the bar. NGC 7741 is a late-type (SB(s)cd) barred spiral with strong asymmetry in the bar, a characteristic which is actually fairly typical of Sd-Sm spirals (de Vaucouleurs & Freeman 1972). To deal with it, we took advantage of the fact that NGC 7741 has no bulge, and chose a center for the Fourier analysis based on the faintest discernible isophotes of the

bar. With such a center, the odd Fourier terms in the bar go to zero near the bar ends. In this circumstance, we can define the bar by even and odd Fourier terms and allow for its asymmetry. We have not accounted for a slight asymmetry in the bars of two other cases, NGC 972 and NGC 7479, because these have bright central regions and the effect is less important.

The success of bar/spiral separation depends on the quality of the near-infrared images. In our case, the WHT images are sufficiently well-exposed that noise levels are minimal in the outer parts of the images. Very bright star-forming regions were removed from the images to minimize their impact. These could have a different mass-to-light ratio than the surrounding old disk stars, and could give false torque amplitudes.

Application of the BBK method is not automatic and requires some iteration for the best choice of the radii r_m. Plots of I_m/I_0, the amplitude of the mth Fourier component relative to the $m=0$ component, were initially made for each galaxy and were evaluated by eye. The most reliable extrapolations were chosen by examining the resulting bar+disk and spiral+disk images. Poor choices of extrapolation would sometimes leave artificial depressions in the spiral+disk image, especially near the ends of the apparent bar. The final extrapolations used are those which provided the cleanest-looking separations. BBK estimated the errors on Q_b and Q_s due to extrapolation uncertainties, and showed that a $\pm 10\%$ uncertainty in the choice of r_2, the radius of the maximum of the dominant $m=2$ term, can lead to a $\pm 4\%$ uncertainty in Q_b and $\pm 10\%$ uncertainty in Q_s, at least for NGC 6951. We expect that this is a reasonable estimate of the uncertainty for the other galaxies in our sample as well (see section 3.2).

We show Fourier extrapolations for the 12 sample galaxies that required bar/spiral separation in Figure 8. (The ones that did not require such separation, NGC 908, 1058, 6643, 7217, and 7606, did not show a measurable bar signal.) In these plots, the curves are the relative intensity amplitudes, and only the lower order terms are shown (the actual analysis used terms up to $m=20$ as in BBK). The symbols show the mappings (interpolations and extrapolations) used for the bar. Except for NGC 1255, NGC 7723, and NGC 7741, the mappings are symmetric around a radius r_m.

For $r < r_m$, the rising relative amplitudes are used as observed, while for $r > r_m$, the amplitudes are extrapolated as the exact reverse of the rise. For NGC 1255, NGC 7723, and NGC 7741, the observed amplitudes already decline past r_m, and in these cases a smaller amount of extrapolation was needed.

These curves show some of the different characteristics of the bars in the sample galaxies. For example, both NGC 1365 and NGC 1433 have bars that can be extrapolated with relatively flat-topped $m=2$ profiles. Although the bar is nothing more than a weak oval in NGC 1255, it still shows a distinct signature in the $m=2$ profile that required little extrapolation. The bar is stronger in NGC 7723, but it dominates the amplitudes inside $r=25''$ and required little extrapolation past r_m. In NGC 7479, the bar and strong spiral produce a double-humped $m=2$ profile, with one hump corresponding to the bar and the other hump corresponding to the spiral. NGC 7741 shows an asymmetric $m=2$ profile.

Bar/spiral separation is most reliable when the bar has a relatively constant position angle in the disk. Figure 8 shows plots of the $m=2$ Fourier phase ϕ_2 as a function of radius for the same 12 galaxies as in Figure 8. The solid vertical lines show the radius, $r(Q_b)$, of the bar maximum from the force ratio maps (see Table 2). These show that the assumption of a constant bar phase is fairly good for the more strongly barred galaxies in the sample, but is less good for the weakly-barred ones. Nevertheless, the extrapolations still produce reasonable separations even for the weaker cases.

Figure 8 shows plots of the rotation curves predicted from the light distribution for each sample galaxy except NGC 7217 (see Buta et al. 1995 for a detailed study of this galaxy). These curves are derived from the $m=0$ component of the gravitational potential as $V = \sqrt{r d\Phi_0/dr}$ and are normalized to the maximum values. The curves look relatively typical of high luminosity spirals.

Figures 4 and 5 show the analysis images and ratio maps, respectively, for the 12 sample galaxies requiring bar/spiral separation. Three images are shown for each galaxy (following BBK): the $m=0$-20 Fourier sum image, the separated bar+disk image, and the separated spiral+disk image. In all cases except NGC 1808, the bar or oval has been

rotated to the approximate horizontal position. For a classical barred spiral like NGC 1365, Figure 4 shows that the extrapolations in Figure 8 produce a fairly clean separation of the bar and the strong spiral. The ratio maps for NGC 1365 in Figure 5 show a very regular pattern of alternating force maxima/minima for this galaxy. In the case of NGC 1433, the extrapolations in Figure 8 also produced a clean separation, but the separated spiral is an oval ring-shaped pattern. Hence, the spiral shows a butterfly pattern similar to the bar. The remaining galaxies each show distinctive characteristics in both the images and ratio maps, but the main point is that the separations appear to be reasonable representations of the galaxies. In the cases of NGC 1255 and 6814, where the bar is nothing more than an $m=2$ oval, the four maximum points lie at about $\pm 40°$-$45°$ to the bar axis, while for the more strongly-barred cases, these points lie much closer to the bar axis. As noted by BB01, higher order terms in the bar potential cause the maximum points to lie closer to the bar axis.

Several of the more highly inclined galaxies in our sample, NGC 908, 972, 5033, 6643, and 7606, required bulge/disk decompositions in order to minimize the effects of bulge "deprojection stretch." The idea is to model the bulge profile, subtract off the bulge from the 2D images, deproject the residual disk light, and then add the bulge back to the deprojected disk light. Since none of these five galaxies is strongly barred, one-dimensional decomposition techniques were adequate for our purposes. We used either the Kent (1986) iterative method or $r^{\frac{1}{4}}$ bulge and exponential disk decompositions (e.g., Kormendy 1977).

The bar separation is perhaps less certain for NGC 5033 than for the other galaxies. The bulge decomposition left some residual zones of lower intensity around the galaxy minor axis. A small bar is found in the inner regions, but its ratio map is affected by the decomposition uncertainties. The ratio map also highlights the bar-like nature of the spiral in this galaxy.

Of the strongly barred spirals with bright centers, the asymmetry in NGC 7479's bar left a residual pattern in the spiral plus disk image. One sees a low intensity region on one side of the center, and a higher intensity region on the other side. Ignoring this asymmetry will not affect Q_b too much

in this case, since Q_b is based on an average of the maximum points in the four quadrants, but will cause us to underestimate the scatter in these maximum points.

Our refined procedure for NGC 7741 accounts for the asymmetry in the bar very well, but leaves a sharp edge in the area around the bar ends. This has very little impact on Q_b, but Q_s could have a larger uncertainty because of it.

From the separated ratio maps, we derived plots of the maximum force ratio, $Q_T(r) = |F_T/F_{0R}|_{max}$ as a function of radius r in the galaxy plane. The way these curves are derived is fully described by BBK. At each radius, we locate the force ratio maximum in four quadrants and then average the results. Figure 8 shows the curves for 16 of our sample galaxies, including the ones for which no clear bar signal was detected. In this figure, the radii are normalized to $r_0(25) = D_o/2$, where D_o is the Galactic extinction-corrected face-on blue light isophotal diameter at a surface brightness level of 25.0 mag arcsec^{-2} (RC3). The results for NGC 7217 are not shown since little forcing due either to a bar or a spiral was detected in this object. Most of the signal seen in the force-ratio map is likely to be due to bulge deprojection stretch, and has $Q_T \leq 0.04$ everywhere. Also, NGC 7217 is the most bulge-dominated system in our sample (Buta et al. 1995), and our procedure will not account for this reliably since, like BB01, we have transformed the light distributions into potentials assuming all components have the same vertical scaleheight. For our main analysis we have set $Q_b \approx Q_s = 0$ for NGC 7217.

Table 2 summarizes the results of the separations. Four other sample galaxies, NGC 908, 1058, 6643, and 7606, also had little or no detectable bar, and we have simply set $Q_b=0$ for these. The weak ovals in NGC 1255 and 6814 were easily separated from their spirals. The remaining galaxies have a range of bar strengths up to $Q_b=0.61$ in NGC 1530. Owing to a limited field of view, the spiral parameters for NGC 1808 are more uncertain than the listed errors imply.

The radii of the maximum relative torques tend to be well inside the standard isophotal radius, for both bars and spirals. For the seven objects in Table 2 having $Q_b > 0.25$, $< r(Q_b)/r_0 > = 0.24\pm 0.09$ (s.d.) and $< r(Q_s)/r_0 > = 0.42\pm 0.09$

(s.d.). For these same galaxies, $< r(Q_b)/r(Q_s) > = 0.57\pm0.13$ (s.d.), so that the maxima tend to be well-separated on average.

3.2. Uncertainties

The main uncertainties in the GTM are due to the uncertainties in the assumed vertical scale-height h_z, variations in the mass-to-light ratio (both due to dark matter or stellar population differences), the adopted orientation parameters (inclination, line of nodes), the bulge deprojection stretch, the bar thickness, the sky subtraction, and the galaxy asymmetry. In addition to these, bar/spiral separation involves uncertainties due to the method of extrapolation. For the more highly inclined galaxies in the sample, we have minimized bulge deprojection stretch using bulge/disk decomposition.

BLS show that the uncertainties in maximum relative torques average about 12% due to uncertainties in the vertical scaleheight. A nonconstant vertical scaleheight in the bar could lead to a further 5% uncertainty in Q_b (Laurikainen & Salo 2002). Uncertainties in galaxy inclinations lead to an inclination-dependence in the uncertainty in Q_b or Q_s. For an error of $\pm5°$ in inclination i, the error in maximum relative torques ranges from 4% for $i \leq 35°$ to 20% for $i \geq 60°$. An uncertainty of $\pm4°$ in line of nodes position angle ϕ has less of an impact, ranging from 4% for $i \leq 35°$ to 11% for $i \geq 60°$. Typical sky subtraction uncertainties on the WHT images could lead to an additional 3.5% uncertainty in Q_b and 5% uncertainty in Q_s (BBK). Finally, uncertainties in the bar extrapolations and in the symmetry assumption of the relative Fourier intensity amplitudes can lead to an additional 4% uncertainty in Q_b and an 11% uncertainty in Q_s (BBK). Table 2 lists the total uncertainty on each parameter from this analysis.

For NGC 1365, the uncertainty in the orientation parameters may be larger than we have assumed. Jorsater & van Moorsel (1995) analyzed an HI velocity field of NGC 1365 and concluded that circular motions may be reliable only between radii of $120''$ and $240''$, where the kinematic position angle and inclination are relatively constant. The kinematic position angle, $220°$, agrees well with the RC3 value of $212°$. However, the kinematic inclination of $40°$ significantly disagrees with the nearly $58°$ inclination implied by the RC3

logarithmic isophotal axis ratio of $logR_{25}=0.26$. Since the bar of NGC 1365 is nearly along the galaxy's minor axis, the derived torque parameters will be sensitive to this disagreement.

The impact of dark matter on maximum gravitational torques for the OSU bright galaxy sample was shown by BLS to be fairly small, especially for those galaxies more luminous than $L_*=2.5\times10^{10}$ $L_\odot$ in the B-band (corresponding to $M_B^o=-20.5$). Because the galaxies in the OSU sample are on average luminous, massive systems, the correction to Q_g was generally less than 10% with an average of about 5%. Our sample here has similar characteristics, with an average luminosity of $L_B=L_*$. The maximum relative gravitational torques in both the bar and the spiral regions tend to lie in the bright inner regions of the galaxies, where the dark halo contribution is small in such luminous galaxies. Thus, it is likely that dark matter has only a minimal impact on our results.

The stellar mass-to-light (M/L) ratio is a separate issue that could impact gravitational torque calculations. Bell & de Jong (2000) used simple spectrophotometric evolution models of spiral galaxies to show that stellar M/L variations can, in fact, be significant, even in the K-band. They present simple relations between color index and the M/L correction for a given passband. However, we cannot make a reliable deduction from their analysis of the error committed by ignoring these variations. Reddening can be significant in color index maps, and would invalidate any M/L corrections from the Bell & de Jong relations in some regions, such as bar dust lanes. Also, tests we have made with $V - K_s$ color index maps of NGC 1530 and NGC 7723 indicate that the near-IR spirals are decoupled from the optical spirals (see section 6) and are not necessarily much bluer than bars, implying that the mass-to-light ratios of the spirals might not be very different from those of bars. However, interbar and interarm regions can be bluer than these features, implying that we could be underestimating Q_b and Q_s slightly. Since our sample is defined by intermediate to late-type spirals, it is likely that Q_b and Q_s are affected by stellar M/L variations in a similar manner for each galaxy, thus largely preserving any relationship between them.

4. Correlation Between Bar and Spiral Strength

With our estimates of separate bar and spiral strengths, we can now check how well these two quantities correlate. Figure 7 shows Q_s versus Q_b assuming constant M/L. For $Q_b < 0.3$, there is only a weak correlation with Q_s, meaning that spirals as strong as $Q_s \approx 0.3$ are possible even in the absence of a bar. However, the strongest spirals in our sample are only associated with bars having $Q_b \geq 0.4$. The error bars tend to be large for these stronger cases in part because two of the galaxies having $Q_b > 0.4$ (NGC 1365 and 1530) have RC3 inclinations close to 60° and one (NGC 7741) has considerable asymmetry in the bar. Figure 7 also suggests that among barred galaxies, stronger bars have stronger spirals. That is, for $Q_b \geq 0.2$, Q_b and Q_s are linearly correlated.

5. Other Indicators of Bar and Spiral Strength

In addition to gravitational torques, the relative importance of bars and spirals can be assessed in a variety of different ways. For example, the deprojected ellipticity of a bar is thought to be a good indicator of bar strength (e.g., Martin 1995), based on the theoretical study by Athanassoula (1992). Abraham & Merrifield (2000) have refined this idea using an automated analysis of two-dimensional surface brightness distributions and a rescaled bar ellipticity parameter called f_{bar} (Whyte et al. 2002). However, bar ellipticity is an incomplete measure of bar strength since the latter also depends on the total mass of the bar (Laurikainen, Salo, & Rautiainen 2002).

Other estimates of bar importance include the bar-interbar contrast and the amplitude of the $m = 2$ Fourier component of the bar. Similarly, the arm strength can be assessed through the use of arm-interarm contrasts. We used the deprojected images to make these estimates for our sample galaxies. Arm classes (flocculent, multiple arm, and grand design; Elmegreen & Elmegreen 1982) were assigned to the galaxies according to their deprojected K_s-band appearance, as indicated in Table 3; some assignments differ from their original classification in the B-band (e.g., Elmegreen & Elmegreen 1987). Intensity cuts were made along the major axis of the discernible

bars (using PVECTOR in IRAF) in order to determine their radial profiles. Bars with constant surface brightness profiles are labeled "flat" in the table, while bars with decreasing profiles are labeled "exponential" (as discussed in Elmegreen & Elmegreen 1985). The lengths of the bars were determined using a program, SPRITE, which fits ellipses to isophotes via least-squares (see Buta et al. 1999). Bar length is taken to be the major axis length at maximum ellipticity, close to where the position angle begins to change. The maximum ellipticities ϵ_b and bar radii r_{bar} (relative to the extinction-corrected isophotal radius from RC3) are given in Table 3. In addition to maximum ellipticities and bar radii from the full images, we also derived these parameters from the *separated bar images*. This is useful for those more strongly barred spirals where the brightest parts of the arms lie very close the bar ends. These are listed as r'_{bar}/r_0 and ϵ'_b in Table 3.

Comparisons between $r(Q_b)/r_0$, $r(Q_s)/r_0$, and r_{bar}/r_0 indicate that $r(Q_s) \approx r_{bar}$ in several of the more strongly barred cases where the inner parts of the spirals affect the isophotal bar fit. However, $r(Q_s) > r'_{bar}$ in all cases.

The deprojected galaxies were transformed into polar images, with gray scale intensities for radius versus azimuthal angle. The bar-interbar amplitude at $0.7r_{bar}$ was estimated from intensity profiles parallel and perpendicular to the bar. Also, azimuthal intensity cuts with a width of three pixels were made from the polar images at radii chosen to be at 0.25 and 0.50 times the standard isophotal radius. From these profiles, the magnitude differences between the bars and the interbar regions or between the arms and the interarm regions were determined for each galaxy, where

$$\text{Contrast(mag)} = 2.5 log(I_{peak}/I_{disk})$$

for $I_{peak} =$ bar or arm intensity and $I_{disk} =$ interbar or interarm intensity. We label the contrast parameters as A_{bar}, $A_{0.25}$, and $A_{0.50}$, respectively. The results are compiled in Table 3.

Fourier transforms for the $m=2$ components of the intensity cuts at $0.7r_{bar}$ were made using the equation

$$F(2) = \sqrt{[\sum I(\theta)sin(2\theta)]^2 + [\sum I(\theta)cos(2\theta)]^2}/\sum(I(\theta))$$

7

where $I(\theta)$ is the intensity at each azimuthal angle θ (ranging from $0°$ to $360°$), and the sums are over all angles. These are also tabulated in Table 3.

The results reveal several correlations among these parameters. The bar-interbar contrast A_{bar} scales in a nearly linear fashion with Q_{b}, but with a considerable scatter at large A_{bar}, as shown in Figure 8a. The bar ellipticity also correlates with bar torque, as shown in Figure 8b, although the relation is not linear. This is fully consistent with the results of Laurikainen, Salo, & Rautiainen (2002), who derived this same correlation from images of more than 40 galaxies from the Two Micron All-Sky Survey (2MASS). For $Q_{\mathrm{b}} < 0.4$, the correlation between ϵ_b and Q_{b} is fairly good, while for $Q_{\mathrm{b}} > 0.4$, the correlation is weaker in the sense that small changes in ϵ_b can correspond to large changes in Q_{b}. The correlation is only slightly improved when ϵ_b' is used. The Fourier strength parameter $F(2)$ correlates with Q_b (with some scatter at large torque), as shown in Figure 8c. These results indicate that the bar-interbar contrast, ellipticity, Q_{b}, and $m{=}2$ Fourier component all provide reasonable measures of bar strength, especially for the weaker bars.

The bar-interbar contrast increases with increasing bar radius, as shown in Figure 8d, where A_{bar} is plotted versus the fractional bar radius r_{bar}/r_0. Furthermore, the bar torque is stronger for flat bars (average value of Q_{b} is 0.43±0.14 for 6 objects) than for exponential bars (0.28±0.16 for 4 objects). These results are consistent with previous K-band studies, which indicated that flat bars are both longer and stronger than exponential bars (Elmegreen & Elmegreen 1985, Regan & Elmegreen 1997). The previous studies also found that earlier spiral types tend to have flat strong bars and later types tend to have exponential weak bars, although a correlation with Hubble type is not obvious in the present small sample. However, correlations of maximum relative gravitational torques with Hubble type have been established by Laurikainen, Salo, & Rautiainen (2002), BLS, and Laurikainen, Salo, & Buta (2004). Early-type bars and spirals tend to be weaker than late-type bars and spirals owing to the dilution effect of bulges in early-types. In the present sample, the strongest bar is that in NGC 7741, which also lacks any significant bulge. Thus, the scatter in the correlation between bar

strength and bar length could be influenced by the importance of the bulge.

The arm-interarm contrast $A_{0.25}$ scales with the arm-interarm contrast $A_{0.50}$ (not shown) but is slightly weaker, which is consistent with previous findings that the arm-interarm contrast increases with radius to about mid-disk (Elmegreen & Elmegreen 1985). There is a weak correlation (not shown) between arm strength and Arm Class, with grand design galaxies having stronger spirals than flocculent galaxies. The arm-interarm contrast increases linearly with the maximum relative spiral torque Q_{s}, as shown in Figure 8e. The correlation is poorer for $A_{0.50}$.

6. Dust-Penetrated Classification

We have applied the dust-penetrated classification scheme of Block & Puerari (1999) to each of our sample galaxies. On the basis of deprojected near-infrared images, evolved stellar disks may be grouped into three principal dust penetrated archetypes: those with tightly wound stellar arms characterized by pitch angles at K_{s} of $\sim 10°$ (the α class), an intermediate group with pitch angles of $\sim 25°$ (the β class) and thirdly, those with open spirals demarcated by pitch angles at K_{s} of $\sim 40°$ (the γ bin). To take full cognizance of the duality of spiral structure and decouplings between gaseous and stellar disks, it has been demonstrated (e.g. Block & Wainscoat 1991) that we require *two* classification schemes – one for the Population I disk, and a separate one for the Population II disk. A near-infrared classification scheme can never *replace* an optical one, and vice-versa, because the *current* distribution of old stars strongly affects the *current* distribution of gas in the Population I disk.

For dust-penetrated classification, logarithmic spirals of the form $r = r_o\exp(-m\theta/p_{\max})$ (see Danver 1942) are employed in the decomposition. The amplitude of each Fourier component is given by (Schröder et al., 1994)

$$A(m,p) = \frac{\Sigma_{i=1}^{I}\Sigma_{j=1}^{J}I_{ij}(\ln r, \theta)\exp\left(-i(m\theta + p\ln r)\right)}{\Sigma_{i=1}^{I}\Sigma_{j=1}^{J}I_{ij}(\ln r, \theta)}$$

where r and θ are polar coordinates, $I(\ln r, \theta)$ is the intensity at position $(\ln r, \theta)$, m represents the

number of arms or modes, and p is the variable associated with the pitch angle P of a given m-mode, defined by $\tan P = -\dfrac{m}{p_{\max}}$. We select the pitch angle of the dominant m-mode to define the dust-penetrated pitch angle classes described above. Of course, the spiral arms in barred galaxies often depart from a logarithmic shape. As noted by Block et al. (2001), the arms may break at a large angle to the bar and then wind back to the other side, as in a "pseudoring." We minimize the impact of non-constant pitch angle due to rings or pseudorings angles by excluding from our analysis the bar regions of the galaxies in question, and by restricting the fits to a limited range in radius.

To illustrate what the Fourier method is extracting, we show in Figure 10 $m=2$ inverse Fourier transform contours superposed on our deprojected K_s image of NGC 1530. This galaxy has a very open two-armed spiral breaking from near the ends of its bar. The dominant m-mode is in this region, and the contours are a reasonable representation of the pitch angle of the arms.

Table 4 summarizes the results of our pitch angle analysis. The radius ranges used for the fits are listed in column 5, except for NGC 1365 and 1433 whose classifications are from Buta & Block (2001). We continue to find a ubiquity of low order $m = 1$ and $m = 2$ modes in this sample, consistent with earlier studies (e.g. Block & Puerari 1999). The most uncertain classifications are for NGC 1808 and NGC 5033, where the field of view limits the part of the main spiral that we can see.

Under very special circumstances, dominant modes with m greater than 2 may develop within the modal theory of spiral structure. Block et al. (1994) and Bertin (1996) hinted that in a *gas-rich* system, some dominant higher-m modes should develop, and this might also induce some response in the stellar disk, for the stronger cases. Furthermore, non-linear modes may couple and again give rise to higher-m structures: $m = 2$ and $m = 1$ combine to give $m = 3$, $m = 2$ and $m = 2$ combined to give $m = 4$, etc. (Elmegreen, Elmegreen, & Montenegro 1992; Block et al., 1994 and G. Bertin, private communication). We use the terminology H3 and H4 for these third and fourth harmonics, to assist with easy visualization of their evolved disk morphologies.

Finding examples of true three- and four-armed spiral galaxies in the near-infrared is a great challenge, requiring the investigation of many galaxies to encounter one or two unambiguous cases. A good example of an $m = 4$ stellar disk in the present study is NGC 6814, while a previously published example is ESO 566−24 (Buta et al. 1998; Rautiainen et al. 2004).

We also note that early Hubble type galaxies (e.g. NGC 972, Sab) can present very wide open arms in the near-infrared; NGC 972 belongs to the γ class. Three other examples are NGC 1808 (of RC3 type Sa but of dust penetrated arm class γ), NGC 1530 and NGC 1365 (both Hubble type SBb; near-infrared arm class γ). Conversely, it is also possible for spirals, classified as late type in the optical regime, to have arms in the near-infrared which are not very wide open (e.g. NGC 908 and NGC 1058 are of Hubble type Sc, but both belong to the more tightly wound β bin: see Table 4).

The present study continues to illustrate decouplings between gaseous and stellar disks and the great advantage of dust-penetration. In the optical, NGC 972 is classified as flocculent by Elmegreen & Elmegreen (1987; see also Table 3). The photograph reproduced by Sandage & Bedke (1994) in panel 148 fully supports the flocculent designation. Sandage & Bedke (1994) note that the optical image of NGC 972 *"is dominated by the heavy dust lanes crossing the near-side of the high-surface-brightness bulge"*. In the near-infrared, NGC 972 presents a principally two-armed spiral; the dominant harmonic is $m=2$. Its grand design, two-armed, evolved stellar disk appears to be completely decoupled from its fleece-like flocculent Population I gas disk. While many optically flocculent spirals may still present a flocculent appearance in the near-infrared (Elmegreen et al. 1999), decouplings of the two components, when present, are indeed very striking.

NGC 1808 is famous for its dust lanes which appear to radiate almost perpendicularly to the major axis. Sandage & Bedke (1994) note in their panel 193, that *"the central region of NGC 1808 provides what appears to be direct evidence of a galactic fountain composed of narrow dust lanes perpendicular to the plane."* The near-infrared imaging successfully penetrates the dust in this SABa spiral, yielding an inner pair of grand design, wide-open arms (the dominant harmonic in NGC 1808 is $m=2$). In this case, bar/spiral sep-

aration has the added uncertainty that the bar position angle is not constant (see Figure 8) and treats the wide-open spiral as part of the bar. Also in this case, there is a strong *coupling* between the gas and star-dominated components, although the inner near-infrared morphology is far more regular.

We use Table 1 of BB01 to define three gravitational torque classes: the total torque class based on Q_g, the bar torque class based on Q_b, and the spiral torque class based on Q_s. The dust-penetrated type (DP-type), written in the form "harmonic class-pitch angle class-bar torque class" following BB01, is given in the last column of Table 4. Except for NGC 7741, *the highest spiral torque classes all belong to the highest pitch angle class, γ.* Six of the galaxies could not be assigned a DP-type.

7. Discussion

The theory of bar-driven spirals is somewhat controversial. Kormendy & Norman (1979) showed that of 33 galaxies having differential rotation and global spiral structure, nearly 80% are barred and likely to have their spirals driven by the bars. The implication was that bars and spirals would have the same pattern speeds. However, Sellwood & Sparke (1988) showed that in n-body numerical simulations where an initially unstable disk forms both a bar and a spiral, the spiral has a lower pattern speed than the bar. Sellwood & Wilkinson (1993) suggested that the quadrupole moment of a realistic bar falls off too rapidly to drive the spirals well beyond the ends of the bar. In this circumstance, the spiral could be an independent instability, or a driven response to a resonance interaction between the bar and spiral. Tagger et al. (1987) and Yuan & Kuo (1997, 1998) have shown that resonance interactions between the bar and the spiral can be an efficient mechanism of wave amplification.

The question of whether spirals and bars corotate can be answered in some cases by the observed alignment of resonance rings. Inner rings and pseudorings in SB galaxies tend to be aligned parallel to bars, while outer rings and pseudorings may be aligned parallel or perpendicular to bars (Kormendy 1979; Schwarz 1984; Buta 1986, 1995). The morphologies of the various ring types

suggest they are driven by bars: inner rings often have pointy oval shapes, indicating a connection with the inner 4:1 ultraharmonic resonance (UHR, Buta & Combes 1996; Salo et al. 1999), while outer pseudorings have three distinctive morphologies that suggest a connection to the outer Lindblad resonance (OLR). These are the R'_1, R'_2, and $R_1 R'_2$ morphologies known as the "OLR subclasses" (Buta 1985, 1986, 1995; Buta & Crocker 1991). The first two types were predicted by Schwarz (1981) from test-particle simulations as being possibly due to differences in the gas distribution around the OLR, while Byrd et al. (1994) showed that the three morphologies may be connected in an evolutionary manner.

Since resonance rings probably develop from the secular evolution of spiral patterns (Schwarz 1981; Byrd et al. 1994; Rautiainen & Salo 2000), the frequent alignments suggest that the spirals that form the rings are driven by the bars at the same pattern speeds. Buta & Combes (1996) further argue that the co-existence of several rings in the same galaxy, showing shapes and alignments that are compatible with periodic orbits near resonances (e.g., NGC 3081, Buta & Purcell 1998), speaks against the existence of several patterns with different pattern speeds. Salo et al. (1999) show that a model that assumes the bar and spiral co-rotate can fit the morphology and the velocity field of the early-type ringed galaxy IC 4214.

The situation is a little different with the central regions of barred galaxies. Here it is possible for the primary bar to induce enough mass flow into the central kiloparsec to cause an inner bar instability, leading to formation of a secondary bar with a different pattern speed (Pfenniger & Norman 1990). Support for the idea of a different pattern speed comes from studies of relative primary bar, secondary bar position angles (e.g., Buta & Crocker 1993; Wozniak et al. 1995).

Rautiainen & Salo (2000, hereafter RS) have reconsidered ring formation in n-body models with dissipatively colliding test particles. These models show the same features as previous test-particle models except that with the self-gravitating stellar disk, additional spiral modes can develop in the same manner as in Sellwood & Sparke (1988). RS consider how these modes, which often have a pattern speed less than that of the bar, affect the morhology and formation of outer rings and pseu-

dorings. The OLR subclasses of outer rings and pseudorings still form in these models, but cyclic changes between the morphologies can occur due to the influence of the modes with a lower pattern speed. If the influence of the lower pattern speed modes is significant enough, RS show that misalignments may be possible. Observed misalignments between inner and outer rings and bars are rare but do occur (Buta 1995; Buta, Purcell, & Crocker 1995).

The only prominent ringed galaxies in our sample are NGC 1433 and NGC 7723. Of these, NGC 1433 shows many features in common with test-particle simulations, including a highly elongated and aligned inner ring likely connected with the inner UHR, an R'_1 outer pseudoring likely connected with the OLR, a misaligned nuclear ring, and two secondary spiral arcs, or plumes, in the vicinity of the outer UHR (Buta et al. 2001). Elmegreen & Elmegreen (1985) argue that a bar like that in NGC 1433 could still be growing through the slow loss of angular momentum to the stellar spiral. In NGC 7723, deprojection of a blue-light image indicates that the inner ring is a nearly circular feature from which a prominent multi-armed spiral pattern emerges. This galaxy does not fit into available test-particle simulations nearly as well as does NGC 1433.

We can see in the plots in Figure 8 that some of the bar torques in our sample are weak in the spiral region, as predicted by Sellwood & Wilkinson (1993). This is the case for NGC 972, 1255, 5033, and 6814. This may also be true in the Milky Way. Our Galaxy has a bar about 1.5 kpc long which generates the 3 kpc arm and perhaps makes the bulge, which is clearly bar-like and about the right length (see, e.g, Cole & Weinberg 2002). Corotation is at $\approx$3 kpc. The spirals outside this radius, which include the local spiral, the Sgr-Carina spiral, and the Perseus spiral, may be independent of the bar. This means their pattern speed is unrelated to the bar pattern or perhaps related in a complex way through resonant excitation. In either case, the bar strength and the spiral arm strength should not be simply related. For resonance excitation, even a weak perturbation can cause a strong response.

Another test of the corotation of bars and spirals concerns the place in azimuth where the inner part of the spiral lies relative to the bar. If the pattern speeds are different or the bar and spiral are unrelated, then the distribution of azimuths for these inner-limit spiral points should be uniform. If all spirals end in their inner regions at the same angular distance from the end of the bar, then the bars and spirals are probably related. To provide a preliminary answer to this question, we examined the twelve barred galaxies in our sample and visually estimated θ_S, the angle between the bar and the inner-limit spiral points, for each prominent spiral arm in each galaxy. Table 3 compiles $< |\theta_S| >$, the average over the prominent arms, and Figure 9 shows how this average correlates with Q_b. The plot shows that for all but two of the galaxies, the spirals appear to begin within $20°$ of the bar axis. The two objects having $< |\theta_S| >$ $> 40°$ are NGC 5033 and 7723, the latter having three spiral arms forming part of the inner ring. Thus, for none of the most strongly barred galaxies in our sample does the near-IR spiral appear to begin at a large intermediate angle to the bar axis. However, in blue light, the situation can be different. For example, both NGC 1530 and 6951 could be interpreted as having serious mismatches between the ends of the bar and the beginnings of the spiral. On the other hand, the weak inner pseudorings in these two objects are made from arms that break from the ends of the bar and wrap around the other ends.

8. Conclusions

From a sample of 17 bright spiral galaxies having a range of bar and spiral morphologies and Hubble types, we find the following from K_s-band images:

1. Bars and spirals can be effectively separated using a Fourier-based image analysis technique (BBK). From this separation, we can quantify the bar and spiral strengths in terms of tangential-to-radial force ratios. In the sample, bar strengths Q_b range from 0 to 0.75 while spiral strengths Q_s range from 0 to 0.46.

2. The spiral strength Q_s correlates with Q_b in a nonlinear fashion: spirals form in non-barred galaxies so Q_s is independent of Q_b when $Q_b < 0.3$, but spiral strengths increase linearly with bar strengths when bars are present, for which $Q_b \geq\sim 0.3$. The effect is not an artifact of stellar M/L variations or dark matter in these high lu-

minosity spirals. If bars and spirals grow together in a global disk instability, then the linear relation between their strengths imply they have about the same growth rates.

3. The bar-interbar contrast A_{bar} and the deprojected bar ellipticity ϵ_b correlate with Q_b, with a smaller scatter for ϵ_b. The arm-interarm contrast also correlates with Q_s, with a better correlation for the contrast measured at a radius of $0.25r_{25}$ compared to $0.5r_{25}$. Strong bars tend to be longer relative to the galaxy isophotal radius. This length-strength correlation may be the result of bar elongation over time as more and more stellar orbits join the bar potential (see simulations in Combes & Elmegreen 1993).

4. Dust-penetrated classifications indicate that the strongest bars with the strongest spirals tend to have the most open spiral arms. Their pitch angles are $40°$ or more and their pitch angle class is γ. The openness of a spiral arm depends on the relative size of the Toomre (1964) length, $2\pi G\Sigma/\kappa^2$ for total disk column density Σ and epicyclic frequency κ. This length is approximately the separation between the arms. If this length is large compared to the radius, then the arms are very open. The ratio of the Toomre length to the galaxy radius is approximately the ratio of the disk mass to the halo mass. Thus open spirals have relatively massive disks (see also Bertin et al. 1977; Elmegreen & Elmegreen 1990). Our observations imply that the most massive disks have the strongest bars and spirals. This suggests that bars and spirals form together in a global disk instability.

5. The correlations between the maximum relative gravitational torques of the bars and spirals and between a number of other measures of bar and spiral amplitudes, in addition to the small angular displacements between the ends of the bars and the inner parts of the spirals, and the alignments of most resonance rings with their bars, all suggest that the bars and spirals in most of our sample have shared the same pattern speeds for cosmological times. In these cases, the bar and spiral corotation radii are the same. Other cases with more irregular ring structures or no evident correlations between bar and spiral strengths or alignments could have their spirals excited either independently of the bar, or excited at a higher order resonance, giving the bars and spirals different pattern speeds and no correlation in structure. The Milky Way is apparently in this latter category.

These conclusions do not necessarily apply to SB0 galaxies, which have strong bars and weak (or no) spirals. This difference from our present sample illustrates the changing morphology of bar-spiral patterns over time. Our results here suggest that the growth phase of a strong bar-spiral pattern is the result of a combined instability having one pattern speed and one growth rate in a relative massive disk. This growth may be spontaneous or it may follow an encounter with another galaxy. After some time, the bar-spiral growth should slow or stop, but it does this for different reasons in the bar and spiral regions. Bars stop growing when they saturate to very large strengths, placing most of the disk stars within the inner 4:1 resonance inside the bar. The inner stellar population is very hot when this happens, because the stellar orbits are highly non-circular. Spirals stop growing when the stellar disk near corotation also heats up, but for the spirals, the high stellar velocities are more random than for the bar, removing the spiral pattern. The high stellar dispersion also requires a nearly complete conversion of gas into stars so that gas dissipation is absent and young stars with low dispersions no longer form. The result is a relatively strong, squared-off bar with little dust and star formation structure in the disk and very weak or no spiral arms, making the SB0 class.

REFERENCES

Abraham, R. G. & Merrifield, M. R. 2000, AJ, 120, 2835

Athanassoula, E. 1992, MNRAS, 259, 328

Bell, E. F. & de Jong, R. 2000, ApJ, 550, 212

Bertin, G., Lau, Y.Y., Lin, C.C., Mark, J.W.K., & Sugiyama, L. 1977, Proc. Nat. Acad. Sciences USA, 74, 4726

Bertin, G. 1996 in *New Extragalactic Perspectives in the New South Africa*, D. L. Block D.L. & J. M. Greenberg, eds., Kluwer, Dordrecht, p. 227

Block, D. L. & Puerari, I. 1999, A&A, 342, 627

Block, D. L. & Wainscoat, R. J. 1991, Nature, 353, 48

Block, D.L. Bertin, G., Stockton, A., Grosbol, P. Moorwood, A. F. M., & Peletier, R. F. 1994, A&A, 288, 365

Block, D. L., Puerari, I., Knapen, J. H., Elmegreen, B. G., Buta, R., Stedman, S., & Elmegreen, D. M. 2001, A&A, 375, 761

Block, D. L., Puerari, I., Frogel, J. A., Eskridge, P. B., Stockton, A., Fuchs, B. 1999, Ap&SS, 269, 5

Block, D. L., Bournaud, F., Combes, F., Puerari, I., & Buta, R. 2002, A&A, 394, L35

Buta, R. 1985, Proc. Astr. Soc. Australia, 6, 56

Buta, R. 1986, ApJS, 61, 609

Buta, R. 1995, ApJS, 96, 39

Buta, R. & Block, D. L. 2001, ApJ, 550, 243 (BB01)

Buta, R., Block, D. L., & Knapen, J. H. 2003, AJ, 126, 1148 (BBK)

Buta, R. & Combes, F. 1996, Fund. Cosmic Physics, 17, 95

Buta, R. & Crocker, D. A. 1991, AJ, 102, 1715

Buta, R. & Purcell, G. B. 1998, AJ, 115, 484

Buta, R., Purcell, G. B., & Crocker, D. A. 1995, AJ, 110, 1588

Buta, R., Alpert, A., Cobb, M. L., Crocker, D. A., & Purcell, G. B. 1998, AJ, 116, 1142

Buta, R., Laurikainen, E., & Salo, H. 2004, AJ, 127, 279

Buta, R., Purcell, G. B., Cobb, M. L., Crocker, D. A., Rautiainen, P., & Salo, H. 1999, AJ, 117, 778

Buta, R., Ryder, S. D., Madsen, G. J., Wesson, K., Crocker, D. A., & Combes, F. 2001, AJ, 121, 225

Buta, R., van Driel, W., Braine, J., Combes, F., Wakamatsu, K., Sofue, Y., & Tomita, A. 1995, ApJ, 450, 593

Byrd, G., Rautiainen, P., Salo, H., Crocker, D. A., & Buta, R. 1994, AJ, 108, 476

Cole, A. A. & Weinberg, M. D. 2002, ApJ, 574, L43

Combes, F. & Sanders, R. H. 1981, A&A, 96, 164

Combes, F. & Elmegreen, B.G. 1993, A&A, 271, 391

Danver, C.G. 1942, Lund Obs Ann. vol 10

de Grijs, R. 1998, MNRAS, 299, 595

de Vaucouleurs, G. & Freeman, K. C. 1972, Vistas in Astr., 14, 163

de Vaucouleurs, G. et al. 1991, Third Reference Catalog of Bright Galaxies (New York: Springer) (RC3)

Elmegreen, B. G. & Elmegreen, D. M. 1989, ApJ, 342, 677

Elmegreen, B. G. & Elmegreen, D. M. 1985, ApJ, 288, 438

Elmegreen, D. M. & Elmegreen, B. G. 1982, MNRAS, 201, 1021

Elmegreen, D. M. & Elmegreen, B. G. 1987, ApJ, 314, 3

Elmegreen, B.G., Elmegreen, D.M., & Montenegro, L. 1992, ApJS, 79, 37

Elmegreen, D. M. & Elmegreen, B. G. 1990, ApJ, 364, 412

Elmegreen, B.G., Wilcots, E., & Pisano, D.J. 1998, ApJ, 494, L37

Elmegreen, D. M., Chromey, F. R., Bissell, B. A., & Corrado, K. 1999, AJ, 118, 2618

Eskridge, P., Frogel, J. A., Pogge, R. W., et al. 2000, AJ, 119, 536

Jogee, S. et al. 2003, in Maps of the Cosmos, IAU Symposium 216, p. 195

Jorsater, S. & van Moorsel, G. 1995, AJ, 110, 2037

Kent, S. 1986, AJ, 91, 1301

Knapen, J. H., de Jong, R. S., Stedman, S., & Bramich, D. M. 2003, MNRAS, 344, 527

Knapen, J. H., Shlosman, I., Heller, C. H., Rand, R. J., Beckman, J. E., Rozas, M. 2000, ApJ, 528, 219

Kormendy, J. 1977, ApJ, 217, 406

Kormendy, J. 1979, ApJ, 227, 714

Kormendy, J. & Norman, C. A. 1979, ApJ, 233, 539

Laurikainen, E., Salo, H., & Buta, R. 2004a, ApJ, in press

Laurikainen, E., Salo, H., & Rautiainen, P. 2002, MNRAS, 331, 880

Laurikainen, E. & Salo, H. 2002, MNRAS, 337, 1118

Laurikainen, E., Salo, H., Buta, R., & Vasylyev, S. 2004b, in preparation

Lindblad, P. A. B., Lindblad, P. O., & Athanassoula, E. 1996, A&A, 313, 65

Martin, P. 1995, AJ, 109, 2428

Packham, C., Thompson, K. L., Zurita, A. et al. 2003, MNRAS, 345, 395

Pfenniger, D. & Norman, C. A. 1990, ApJ, 363, 391

Quillen, A. C., Frogel, J. A., & González, R. A. 1994, ApJ, 437, 162

Rautiainen, P. & Salo, H. 2000, A&A, 362, 465

Rautiainen, P., Salo, H., & Buta, R. 2004, MNRAS, in press (astro-ph/0305530)

Regan, M. & Elmegreen, D. M. 1997, AJ, 114, 965

Regan, M., Teuben, P. J., Vogel, S. N., & van der Hulst, T. 1996, AJ, 112, 2549

Salo, H., Rautiainen, P., Buta, R., Purcell, G. B., Cobb, M. L., Crocker, D. A., & Laurikainen, E. 1999, AJ, 117, 792

Sandage, A. & Bedke, J. S. 1994, The Carnegie Atlas of Galaxies, Carnegie Inst. of Wash. Publ. No. 638

Sanders, R. H. & Tubbs, A. D. 1980, ApJ, 235, 803

Schröder, M.F.S, Pastroriza, M.G, Kepler, SO and Puerari, I. 1994, A&AS, 108, 41

Schwarz, M. P. 1981, ApJ, 247, 77

Schwarz, M. P. 1984, A&A, 133, 222

Sellwood, J. A. & Sparke, L. S. 1988, MNRAS, 231, 25P

Sellwood, J. A. & Wilkinson, A. 1993, Rep. Prog. Phys., 56, 173

Tagger, M., Sygnet, J. F., Athanassoula, E., & Pellat, R. 1987, ApJ, 318, L43

Whyte, L., Abraham, R. G., Merrifield, M. R.,

Eskridge, P. B., Frogel, J. A., & Pogge, R. W. 2002, MNRAS, 336, 1281

Wozniak, H., Friedli, D., Martinet, L., Martin, P, & Bratschi, P. 1995, A& AS, 111, 115

Yuan, C., Kuo, C.-L. 1997, ApJ, 486, 750

Yuan, C., Kuo, C.-L. 1998, ApJ, 497, 689

TABLE 1

PROPERTIES OF THE SAMPLE GALAXIES[a]

Galaxy	Type	$\log D_o$	$\log R_{25}$	B_T^o	Δ (Mpc)	M_B^o	source	Exp. Time (min)
1	2	3	4	5	6	7	8	9
NGC 908	SA(s)c	1.78	0.36	10.35	17.8	−20.9	WHT-INGRID	73
NGC 972	Sab	1.55	0.29	11.48	21.4	−20.2	WHT-INGRID	64
NGC 1058	SA(rs)c	1.51	0.03	11.55	9.1	−18.3	WHT-INGRID	62
NGC 1255	SAB(rs)bc	1.62	0.20	11.26	19.9	−20.2	WHT-INGRID	60
NGC 1365	SB(s)b	2.05	0.26	9.93	16.9	−21.2	CTIO-CIRIM	40
NGC 1433	(R′)SB(r)ab	1.81	0.04	10.64	11.6	−19.7	CTIO-CIRIM	30
NGC 1530	SB(rs)b	1.72	0.28	11.42	36.6	−21.4	WHT-INGRID	48
NGC 1808	(R)SAB(s)a	1.81	0.22	10.43	10.8	−19.7	WHT-INGRID	56
NGC 5033	SA(s)c	2.03	0.33	10.21	18.7	−21.2	WHT-INGRID	16
NGC 6643	SA(rs)c	1.60	0.30	11.14	25.5	−20.9	WHT-INGRID	63
NGC 6814	SAB(rs)bc	1.54	0.03	11.32	22.8	−20.5	WHT-INGRID	60
NGC 6951	SAB(rs)bc	1.68	0.08	10.71	24.1	−21.2	WHT-INGRID	60
NGC 7217	(R)SA(r)ab	1.63	0.08	10.53	16.0	−20.5	WHT-INGRID	64
NGC 7479	SB(s)c	1.63	0.12	11.22	32.4	−21.3	WHT-INGRID	59
NGC 7606	SA(s)b	1.73	0.40	10.88	28.9	−21.4	WHT-INGRID	58
NGC 7723	SB(r)b	1.55	0.17	11.57	23.7	−20.3	WHT-INGRID	48
NGC 7741	SB(s)cd	1.65	0.17	11.43	12.3	−19.0	WHT-INGRID	100

[a]Col. 1: galaxy name; col. 2: de Vaucouleurs revised Hubble type (RC3); col. 3: log of corrected isophotal diamater (units of $0'.1$) at $\mu_B = 25.0$ mag arcsec^{-2} (RC3); col. 4: log of iosphotal axis ratio at $\mu_B = 25.0$ mag arcsec^{-2} (RC3); col. 5: total corrected blue light apparent magnitude (RC3); col. 6: distance in Mpc (Tully 1988); col. 7: absolute blue light magnitude; col. 8: source of image (WHT=William Herschel Telescope; CTIO=Cerro Tololo Inter-American Observatory); col. 9: total on-source exposure time in minutes

TABLE 2

DERIVED TORQUE PARAMETERS[a]

Galaxy	h_z	Q_b	Q_s	Q_g	$r(Q_b)$	$r(Q_s)$	$r(Q_g)$	$r(Q_b)/r_0$	$r(Q_s)/r_0$	$r(Q_g)/r_0$
1	2	3	4	5	6	7	8	9	10	11
NGC 908	379	(0.00)	0.28±0.10	0.28	....	73.0	73.0	....	0.40	0.40
NGC 972	372	0.22±0.06	0.21±0.06	0.24	9.0	29.0	8.0	0.08	0.27	0.08
NGC1058	100	(0.00)	0.09±0.02	0.09	....	18.0	18.0	....	0.19	0.19
NGC1255	482	0.07±0.01	0.15±0.04	0.17	4.5	23.5	76.0	0.04	0.19	0.61
NGC1365	1587	0.40±0.11	0.36±0.11	0.49	118.5	178.0	164.0	0.35	0.53	0.49
NGC1433	581	0.37±0.06	0.23±0.05	0.43	68.0	106.5	69.0	0.35	0.55	0.36
NGC1530	777	0.61±0.16	0.42±0.16	0.73	45.0	65.5	49.0	0.29	0.42	0.31
NGC1808	600	0.22±0.04	0.10±0.02	0.24	70.5	118.0:	73.5	0.36	0.61:	0.38
NGC5033	841	0.07±0.02	0.12±0.03	0.12	8.5	29.5	29.5	0.03	0.09	0.09
NGC6643	383	(0.00)	0.21±0.08	0.21	....	28.0	28.0	....	0.23	0.23
NGC6814	375	0.07±0.01	0.09±0.02	0.10	10.0	44.5	15.0	0.10	0.43	0.14
NGC6951	640	0.28±0.04	0.21±0.06	0.34	31.5	57.5	43.0	0.22	0.40	0.30
NGC7217	566	(0.00)	(0.00)	<0.04	....	....	....	....	....	....
NGC7479	494	0.59±0.10	0.46±0.12	0.71	31.0	50.0	45.0	0.24	0.39	0.35
NGC7606	898	(0.00)	0.08±0.02	0.08	....	42.5	42.5	....	0.26	0.26
NGC7723	508	0.30±0.05	0.12±0.02	0.31	16.0	33.0	16.0	0.15	0.31	0.15
NGC7741	274	0.74±0.22	0.35±0.07	0.77	15.0	46.0	15.0	0.11	0.34	0.11

[a]Col. 1: galaxy name; col. 2: vertical scaleheight in pc; col. 3: relative bar torque parameter (bar strength); col. 4: relative spiral torque parameter (spiral strength); col. 5: gravitational torque parameter (total nonaxisymmetric strength); col. 6: radius (arcsec) of maximum average relative bar torque; col. 7: radius (arcsec) of maximum average relative spiral torque; col. 8: radius of maximum average relative total torque; cols.9-11: same radii as in cols. 6-8, relative to $r_o = D_o/2$, the extinction-corrected de Vaucouleurs isophotal radius.

TABLE 3

SPIRAL AND BAR CONTRASTS, DIMENSIONS, AND SHAPES[a]

Galaxy 1	Arm Class 2	$A_{0.25}$ 3	$A_{0.50}$ 4	A_{bar} 5	r_{bar}/r_0 6	ϵ_b 7	r'_{bar}/r_0 8	ϵ'_b 9	$F(2)$ 10	$< |\theta_S| >$ 11
NGC 908	M	0.59	0.79	....	....	....	....	....	....	.....
NGC 972	F	0.96	1.27	0.53	0.11	0.51	0.10	0.51	....	3:±1:
NGC 1058	F	0.38	0.52	....	....	....	....	....	....	.....
NGC 1255	M	0.56	0.67	0.20	0.06	0.18(exp)	0.06	0.18	....	18±17
NGC 1365	G	....	2.10	2.05	0.53	0.76(flat)	0.50	0.71	0.40	9±4
NGC 1433	G	....	1.78	1.64	0.54	0.70(flat)	0.37	0.65	0.33	8±2
NGC 1530	G	1.67	3.01	2.35	0.43	0.74(flat)	0.33	0.67	0.38	15±5
NGC 1808	G	0.39	0.96	0.69	0.37	0.52(exp?)	0.37	0.52	0.06	.....
NGC 5033	M	0.65	....	....	..	....	....	....	....	67±5
NGC 6643	M	0.73	0.67	....	..	....	....	....	....	.....
NGC 6814	M	0.38	0.76	0.37	0.12	0.25(exp)	0.16	0.27	....	4±3
NGC 6951	G	1.25	1.63	1.15	0.33	0.64(flat)	0.25	0.58	0.22	12±7
NGC 7217	F	0.19	0.34	....	....	....	....	....	....	.....
NGC 7479	G	2.03	1.46	1.47	0.39	0.71(flat)	0.23	0.68	0.93	7±7
NGC 7606	G	0.43	0.33	....	....	....	....	....	....	.....
NGC 7723	M	0.54	0.57	1.02	0.18	0.61(flat)	0.18	0.61	0.11	51±22
NGC 7741	F	1.35	0.94	1.34	0.14	0.73(exp)	0.14	0.73	0.32	7±4

[a]Col. 1: galaxy name; col. 2: spiral Arm Class (Elmegreen & Elmegreen 1987, where F=flocculent, M=multi-armed, G=grand-design); cols. 3,4: the near-IR arm-interarm contrast at 0.25 and 0.50 times the RC3 isophotal radius; col 5: the near-IR bar-interbar contrast at 70% of the deprojected bar radius; col. 6, deprojected bar radius relative to isophotal radius; col 7: deprojected near-IR ellipticity of the bar (in parentheses, exp=exponential-profile bar while flat=flat-profile bar); col. 8: deprojected bar radius relative to the standard (extinction-corrected) isophotal radius, based on the separated bar+disk image; col. 9: deprojected near-IR ellipticity of the bar, based on the same image; col. 10: Fourier near-IR $m=2$ amplitude; col. 11: average inner-limit spiral point angles relative to the bar axis, in degrees.

TABLE 4

DUST-PENETRATED CLASSIFICATION[a]

Galaxy 1	Torque Class 2	Bar Class 3	Spiral Class 4	Radius Range 5	m 6	$|P|$ 7	DP Type 8
NGC 908	3	0	3	24–60	2	28.07	H2β0
					3	38.66	
NGC 972	2	2	2	6–19	2	38.66	H2γ2
NGC 1058	1	0	1	6–12	2	25.20	H2β0
NGC 1255	2	1	2	8–27	2	31.61	H2β1
NGC 1365	5	4	4	.....	2	.....	H2γ4[b]
NGC 1433	4	4	2	.....	2	.....	H2α4[b]
NGC 1530	7	6	4	29–58	2	33.69	H2γ7
NGC 1808	2	2	1	18–48	2	69.44	H2γ2
NGC 5033	1	1	1	10–24	2	28.07	H2β1
NGC 6643	2	0	2	7–41	..	.....	0
NGC 6814	1	1	1	8–36	4	34.82	H4γ1
					2	11.31	
NGC 6951	3	3	2	24–60	2	45.00	H2γ3
NGC 7217	0	0	0	.....	..	.....	0
NGC 7479	7	6	5	24–60	2	33.69	H2γ6
NGC 7606	1	0	1	17–48	2	31.61	H2β0
NGC 7723	3	3	1	10–24	..	.....	3
NGC 7741	8	8	4	22–34	..	.....	8

[a]Col. 1: galaxy name; col. 2: maximum relative gravitational torque class; col. 3: bar torque class; col. 4: spiral torque class; col. 5: radius range (arcsec) for harmonic and pitch angle fits; col. 6: multiplicity of dominant spiral harmonic; col. 7, pitch angle associated with harmonic component m; col. 8: dust-penetrated classification (Block & Puerari 1999; Buta & Block 2001).

[b]Harmonic and pitch angle classes from Buta & Block (2001).

Fig. 1.— Plots of relative Fourier intensity amplitudes as a function of radius for 12 galaxies where bar/spiral separation was needed. Symbols show the extrapolations used for our analysis (see text). For the stronger bar cases, even terms for $m=2$ (solid curve), 4 (dotted curve), and 6 (short dashed curve) are shown. For NGC 1255 and NGC 6814, only the $m = 2$ and 4 terms are shown.

Fig. 2.— Plots of the phase of the $m=2$ Fourier component for the same 12 galaxies as in Figure 1. The solid vertical lines indicate the radius of the bar maximum from Table 2.

Fig. 3.— Predicted axisymmetric rotation curves for 16 of the sample galaxies, assuming a constant mass-to-light ratio at 2.1μm. Each rotation curve is normalized to its maximum V_m.

Fig. 4.— Separated bar and spiral images for 12 galaxies. Three images are shown for each galaxy in the following categories: m=0-20 sum (left), bar+disk (middle), and spiral+disk (right). Each galaxy is identified only in the leftmost of its three images.

Fig. 5.— Separated bar and spiral force ratio maps for 12 galaxies. Three ratios maps are shown for each galaxy in the following categories: m=0-20 sum (left), bar+disk (middle), and spiral+disk (right). Each galaxy is identified only in the leftmost of its three maps.

Fig. 6.— Plots of the average maximum ratio of the tangential force to the mean radial force as a function of radius normalized to the extinction-corrected de Vaucouleurs standard isophotal radius, for 16 of the sample galaxies. The separate curves refer to the bar (dashed curve), spiral (dotted curve), and the m=0-20 sum image (solid curve).
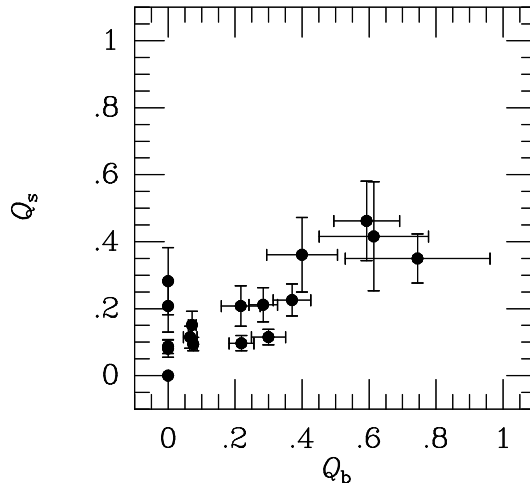

Fig. 7.— Plot of the maximum relative spiral torque, Q_{s}, versus the maximum relative bar torque, Q_{b}. Strong bars and spirals are towards the top and right, respectively.

Fig. 9.— Plot of the azimuthal angle of the beginning of the inner spiral, averaged over two or more arms, versus the bar strength Q_b. The error bars on the angles are average deviations, while those on Q_b are total mean errors.
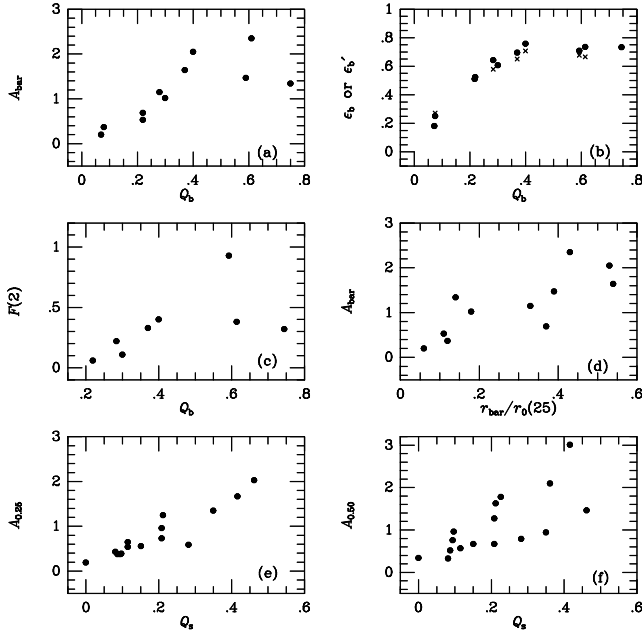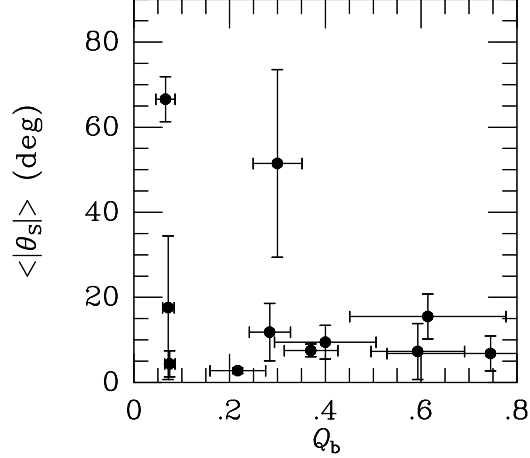

Fig. 8.— Plots of (a) bar-interbar contrast at $0.7r_{bar}$ versus Q_b; (b) bar ellipticity versus Q_b (filled circles are ϵ_b for the full images, while crosses are ϵ'_b for the separated bar images); (c) $m=2$ Fourier transform amplitude versus Q_b; (d) bar-interbar contrast versus bar radius relative to the (extinction-corrected) face-on standard isophotal radius; (e) arm-interarm contrast at 0.25 times the standard isophotal radius versus Q_s; and (f) same as (e), for 0.5 times the standard isophotal radius.

Fig. 10.— Inverse Fourier transform contours of dominant harmonic superposed on a deprojected K_s-band image of NGC 1530.

18

This figure "Fig1page.jpg" is available in "jpg" format from:

http://arXiv.org/ps/astro-ph/0405227v1

This figure "Fig2page.jpg" is available in "jpg" format from:

http://arXiv.org/ps/astro-ph/0405227v1

This figure "Fig3page.jpg" is available in "jpg" format from:

http://arXiv.org/ps/astro-ph/0405227v1

This figure "Fig4page.jpg" is available in "jpg" format from:

http://arXiv.org/ps/astro-ph/0405227v1

This figure "Fig5page.jpg" is available in "jpg" format from:

http://arXiv.org/ps/astro-ph/0405227v1

This figure "Fig6page.jpg" is available in "jpg" format from:

http://arXiv.org/ps/astro-ph/0405227v1

This figure "Fig10page.jpg" is available in "jpg" format from:

http://arXiv.org/ps/astro-ph/0405227v1